Journal of Colloid and Interface Science 702 (2026) 138922

Contents lists available at ScienceDirect

Journal of Colloid And Interface Science

journal homepage: www.elsevier.com/locate/jcis

Fluorine-oxygen dual sites engineered on carbon enable high efficiency in the cycloaddition of carbon dioxide: synergistic effect, density functional theory validation and kinetic modeling

Jianhan Yang [a,b], Jiangnan Huang [a,*], Hao-Fan Wang [b], Hongjuan Wang [b], Hao Yu [b], Yonghai Cao [b,*]

[a] College of Chemistry and Chemical Engineering, Zhongkai University of Agriculture and Engineering, Guangzhou 510225, China
[b] School of Chemistry and Chemical Engineering, Guangdong Provincial Key Lab of Green Chemical Product Technology, South China University of Technology, Guangzhou 510640, China

HIGHLIGHTS

- FCMs were prepared and applied as the catalyst for CO_2 cycloaddition for the first time.
- FCM-500 displayed 94 % carbonate yield in the CO_2 cycloaddition reaction.
- Semi-ionic C—F bond and oxygen-containing functional groups dominated the reaction.
- DFT simulation validate the reaction mechanism.
- A reliable and predictable kinetic model was established.

GRAPHICAL ABSTRACT

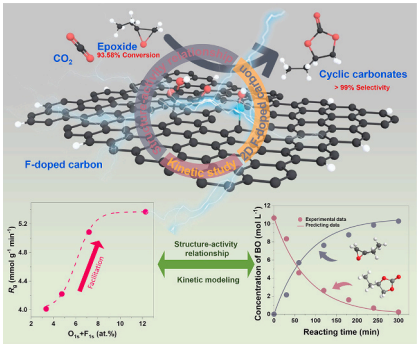

ARTICLE INFO

Keywords:
Carbon catalyst
CO_2 cycloaddition
Fluorine doping
Oxygen-containing group

ABSTRACT

Fluorine (F)-doped carbon materials (FCMs) were one-pot synthesized and applied as the catalysts for the cycloaddition of carbon dioxide (CO_2) towards the cyclic carbonate for the first time. In this process, F dopants and oxygen (O)-containing groups on the carbon surface played a key role in enhancing the activity. The FCM synthesized at 500 °C (FCM-500) with 5.8 at.% F and 6.5 at.% O afforded 94.5 ± 2.5 % conversion, which was much higher than that of FCM synthesized at 800 °C (FCM-800, 78.2 ± 3.8 %) with 0.2 at.% F and 3.1 at.% O. The pseudo-first-order apparent rate constant and activation energy (E_a) of FCM-500 were found as 0.6 h^{-1} and 36.7 kJ mol^{-1}, better than those over FCM-800 (0.3 h^{-1} and 39.6 kJ mol^{-1}). The density functional theory (DFT) simulations revealed that the presence of F dopant and oxygen-containing groups would synergistically enhance the activity. The detailed structure-activity investigation was conducted and revealed that the semi-ionic C—F bonds and oxygen-containing functional groups (hydroxyl, carboxyl, and quinonic carbonyl) on the surface of FCMs acted as the synergistic sites, which positively influenced the CO_2 cycloaddition reaction. Based on these findings, a reliable and quantitative kinetic model with the semi-ionic C—F bonds, carboxyl, and quinonic carbonyl groups as the key sites was established for the FCM-catalyzed reaction system, in which the apparent

* Corresponding authors.
E-mail addresses: huangjiangnan@zhku.edu.cn (J. Huang), meyhcao@scut.edu.cn (Y. Cao).

https://doi.org/10.1016/j.jcis.2025.138922
Received 11 July 2025; Received in revised form 1 September 2025; Accepted 2 September 2025
Available online 3 September 2025
0021-9797/© 2025 Elsevier Inc. All rights are reserved, including those for text and data mining, AI training, and similar technologies.

reaction rate constant was 4.3 × 10^{-2} $mol^{-0.9}$ $L^{0.9}$ min^{-1}, and the reaction orders of 1, 2-butylene oxide (BO), tetrabutylammonium bromide (TBAB), and FCM were 1, 0.6, 0.4, respectively. These kinetic parameters verified the feasibility of predicting the concentration of the substrates under different reaction conditions as well. This study offers a new strategy for the kinetic investigation of the CO_2 cycloaddition reaction catalyzed by the heteroatom-doped carbon catalysts.

1. Introduction

The rapid industrialization leads to the apparent rise of global carbon dioxide (CO_2) levels, sparking serious international environmental concerns. To reduce greenhouse gas emissions and further combat climate change, the ambitious carbon-neutrality goals across different countries were set [1–3]. Among various strategies, converting CO_2 into value-added products is one of the promising ways to tackle this issue. Typically, CO_2 and epoxides as the substrates yielding carbonates under mild conditions is a fascinating approach with the 100 % atom economy, which aligns with green chemistry principles. Carbonates, vital in chemical production like polycarbonates and dimethyl carbonates, have a broad global market with ~7 billion USD by 2030. This technology would lower CO_2 emissions and boost sustainable chemical industry development.

In the past decades, heterogeneous catalysts have garnered increasingly widespread attention in the field of catalytic CO_2 cycloaddition reactions [4,5]. Among them, nanocarbon materials have emerged as a hotspot due to their unique physicochemical properties, including high specific surface area, tunable electronic structure, and high intrinsic catalytic activity [6,7]. Particularly, heteroatom-doped carbon materials, especially N-doped carbons, have demonstrated significant potential in facilitating the CO_2 cycloaddition [8,9]. For instance, Yang et al. applied the hollow N-doped porous carbon with single Zn atoms for the CO_2 cycloaddition [10]. N sites in this process performed as a Lewis base site to enhance the reaction. Based on this, Lepre et al. prepared a carbon material with a high content of N sites (34 wt%) to improve the activity of CO_2 cycloaddition [8]. These studies offered an opinion that N dopants acted as the basic sites while oxygen-containing groups acted as acidic sites, which synergistically promoted the CO_2 cycloaddition. Generally, the doping of heteroatoms into the carbon skeleton would dramatically alter the surface electron density, leading to variations in interactions between the carbon catalyst and substrates [11–13]. Peng and co-workers found that the heteroatoms such as N, S, P, B, etc. in the carbon skeleton usually varied the surface electron density [14–18], noted as n-type and p-type doping [19], which could greatly influence the catalytic activity of carbon catalyst in the selective oxidation of hydrocarbons [15,20,21]. Therefore, the heteroatoms-doping could not only vary the surface acidic/basic property of nanocarbons, but also change the surface electron property [22–24].

In fact, the change of the surface electron density on nanocarbons was ascribed to the electronegativity differences between heteroatoms and carbon atoms [6]. As the most electronegative element, fluorine (F) doping can locally induce a high positive charge at the neighboring carbon atoms, fundamentally regulating the physicochemical properties of carbon materials, including conductivity, thermal stability, and mechanical performance, primarily attributed to the high bond energy of C—F bonds (~ 485 kJ mol^{-1}) [25–31]. For instance, F incorporation induced the transition from sp^2-hybridized carbon to sp^3-hybridized carbon in graphene material, producing more defects with modulated electron density [32], which not only affected material conductivity but also provided abundant active sites, rendering it highly effective in catalysis and adsorption applications. In the field of oxygen reduction reaction (ORR), carbon materials with F dopants exhibited remarkable catalytic activity due to F-mediated regulation of the carbon matrix's electronic structure, which enhanced the adsorption and activation of O_2 molecules [33]. Our previous work demonstrated that F doping into carbons would modulate the surface property of F-doped carbons (FMCs), which enhanced the interactions between FMCs and hexavalent chromium (Cr(VI)) ions [34]. In the field of CO_2 utilization, F doping was also found to modulate the carbon physical structure and enhance the interaction between carbon materials and CO_2. Xie et al. applied F-doped carbon as the electrocatalyst for the CO_2 reduction and displayed a superior kinetics in this reaction [29]. They believed that F doping could induce the positive charge of the neighbor carbon atoms and enhance the adsorption of COOH* on F doped carbon material, thereby facilitating the reaction. Zhao et al. reported that the F doping would greatly enhance the surface electrostatic potential, thus leading to the improved CO_2 adsorption capacity in carbon material [30]. These studies demonstrated that F doping was a promising strategy for CO_2 utilization. However, there is little literature focusing on FMCs for CO_2-epoxides cycloaddition reactions to date.

In this work, FCMs were synthesized via a straightforward one-step calcination method using polyvinylidene fluoride (PVDF) as the precursor. PVDF is a kind of widely used plastic material with a global production capacity of ~350, 000 t/y. The utilization of waste plastic PVDF as the carbon and fluorine sources to prepare FCMs is a resource reuse and meets the requirements of sustainable issues [35,36]. The obtained carbon materials were used as the catalysts to catalyze the CO_2 cycloaddition under solvent-free conditions for the first time, to the best of our knowledge. In this process, the considerable activity of FCMs was observed. Through systematic experimental design and density functional theory (DFT) simulations, the catalytic mechanisms of FCMs in CO_2 cycloaddition reactions were comprehensively investigated. Meanwhile, the kinetics investigations were conducted to establish a reliable kinetic model for FCMs-catalyzed reactions, which was well-predictable for the CO_2 cycloaddition under different reaction conditions.

2. Experimental section

2.1. Materials

Polyvinylidene fluoride (PVDF, MW 20000, 99 %), $Fe(NO_3)_3{\cdot}9H_2O$ (AR), hydrochloric acid (HCl, 35–37 wt%), 1, 2-butylene oxide (BO, >99.0 %), 1, 2-dichlorobenzene (DCB, >99.0 %), tetrabutylammonium bromide (TBAB, >98.0 %), *N*, *N*-dimethylformamide (DMF, >99.5 %) were purchased from Shanghai Aladdin Biochemical Technology Company, China. CO_2 (99.99 %) and N_2 (99.99 %) were purchased from Air Liquide, Guangdong, China. All chemicals were directly used without purification.

2.2. Preparation of carbon catalysts

The FCMs were synthesized via a one-pot pyrolysis process. Typically, 3 g of PVDF and 6 g of $Fe(NO_3)_3{\cdot}9H_2O$ were placed into a beaker, followed by the addition of 100 mL of anhydrous ethanol. The mixture was magnetically stirred until fully dissolved and homogenized. Subsequently, the solution was transferred to an oven at 100 °C for thorough desiccation. The obtained solid was then ground into a fine powder using an agate mortar and transferred into a tube furnace, where the sample was heated to target temperatures (500–800 °C) with a heating rate of 5 °C min^{-1} under a N_2 atmosphere and maintained for 2 h. After cooling down to room temperature, the obtained materials were washed with 1 mol L^{-1} HCl solution, which was then filtered and washed repeatedly with deionized water and ethanol until the pH of the filtrate

was neutral. The final product was dried at 60 °C for 12 h, which was labeled as FCM-T (where T denotes the carbonization temperature). In particular, the product carbonized at 800 °C without acid washing was noted as Fe-FCM-800.

2.3. Characterization

The N_2 absorption/desorption curves, pore diameter, and the Brunauer-Emmett-Teller surface area of the catalysts were tested by the ASAP 2010 (Micromaritics, USA). X-ray powder diffraction (XRD) patterns were obtained using a Multibit auto-injection X-ray diffractometer (X'pert^3 Powder, PANalytical B.V., Netherlands) with Cu-Kα radiation. Transmission Electron Microscope (TEM) images were obtained from the JEM-2100F and JEM-1400 Plus (JEOL Company, Japan). For TEM measurements, a small amount of the catalyst was ultrasonically dispersed in absolute ethanol, and a drop of the suspension was deposited onto a grid coated with an amorphous copper film. Raman spectra were recorded using a microscopy Raman spectrometer (LabRAM Aramis, HJY, France) with an excitation wavelength of 633 nm. Fourier Transform Infrared (FTIR) spectroscopy analysis of all samples was performed using a Nicolet IS50 infrared spectrometer (Thermo Scientific, USA). X-ray photoelectron spectroscopy (XPS) measurements were carried out on a Thermo Scientific K-Alpha spectrometer (ESCALAB 250Xi, Thermo Scientific, USA) equipped with an Al K_α X-ray source, and the binding energies were calibrated using the C_{1s} peak at 284.8 eV. Thermogravimetric analysis (TGA) of all the samples was performed using a NETZSCH STA499C analyzer (NETZSCH, Germany) by heating from 30 °C to 800 °C at a ramp rate of 10 °C min^{-1} with the gas flow mixed with 20 mL min^{-1}Air and 20 mL min^{-1} N_2.

2.4. Catalytic performance

The catalytic activity tests were performed in a batch mode using a 50 mL Teflon-lined stainless-steel micro-autoclave. Typically, 170 mmol of 1, 2-butylene oxide (BO), 10 mmol of 1, 2-dichlorobenzene (DCB, the internal standard), 7.1 mmol of tetrabutylammonium bromide (TBAB), and 400 mg of catalyst were charged into the micro-autoclave, followed by a heating process. Once the desired temperature was reached, the autoclave was pressurized with CO_2 and maintained. When the reaction was completed, the reactor was rapidly cooled down using an ice bath. The obtained mixture was diluted with *N*, *N*-dimethylformamide and then filtered. The liquid sample was analyzed using gas chromatography (Fuli-9790Plus) equipped with a DB-1701 column and a flame ionization detector. The temperature program was set as follows: initial temperature of 85 °C held for 1 min, followed by a heating rate of 15 °C min^{-1} to a final temperature of 265 °C. The injector temperature was set to 250 °C, and the detector temperature was set to 280 °C. Before the reusability testing, the used catalyst was washed repeatedly with ethanol and then dried in an oven at 60 °C overnight. The catalyst was subsequently annealed at 400 °C in an argon atmosphere for 1 h. The average value of the results for each experiment was calculated by taking the mean of the results from three trials.

2.5. Density functional theory (DFT) simulation

To simulate the adsorption behavior on the surface, various graphene planes along with substrates or intermediates were utilized. A periodic system was employed for all calculations, which were conducted using the Dmol3 package with the GGA/PBE exchange-correlation functional [37]. All adsorption energies and energy barriers for stable intermediates on the catalyst surface were determined based on the DFT simulation. For bulk calculations, the k-point sampling of the Brillouin zone was set to 4 × 4 × 1 [38,39]. The convergence criteria for energy, maximum force, and maximum displacement were set to 1 × 10^{-5} Ha, 0.002 Ha/Å, and 0.005 Å, respectively. Additionally, to prevent interactions between periodic configurations, a vacuum space of 15 Å was introduced in the direction perpendicular to the surface.

The adsorption energy (ΔE) of adsorbate (A) on substrate was calculated by the following equation:

$$\Delta E_{ads} = E_{A\text{-Substrate}} - E_A - E_{\text{Substrate}} \quad (1)$$

where the $E_{\text{A-substrate}}$, E_A and $E_{\text{Substrate}}$ were the total energies of the molecule A adsorbed system, the free molecule A and substrate material, respectively. In addition, the more negative the value of ΔE, the more favorable the substrate adsorption to A.

3. Results and discussion

3.1. Characterization and catalytic performance

The process of the FCMs synthesis was illustrated in Fig. 1a, which underwent the one-pot annealing treatment. In this process, the sublimation temperature of PVDF was comparably low, which resulted in a low carbon yield via direct pyrolytic carbonization. To address this, Fe salt was introduced as a precursor for this process under temperatures ranging at 500 to 800 °C. As shown in **Fig. S1a**, FCM-500 exhibited a flake structure with uniformly distributed hollow cavities, originating from the formation of iron nanoparticles as the templates during low-temperature carbonization, which was efficiently removed by acid washing to form the hollow cavities. As the carbonization temperature increases, the density of iron nanoparticles within the FCMs rose, accompanied by thickening of the carbon shells and the emergence of curved hollow cylindrical carbon tubes (**Fig. S1b-d**). This structure variation was attributed to the temperature-dependent carbon thermal reaction of iron [40,41]. Higher temperatures intensified iron-catalyzed carbon reorganization, leading to greater retention of iron-carbon composites and enhanced structural complexity [42]. High-resolution TEM images showed the highly porous flake structure across all the FCMs (Fig. 1c-e). Meanwhile, it was difficult to find Fe nanoparticles in FCM-500 and FCM-600, meaning that most of the Fe nanoparticles were removed during the acid washing process. For the FCM-700 and FCM-800, the apparent Fe nanoparticles were observed (**Fig. S1e-f**). The 0.33 nm of lattice spacing was obtained, corresponding to the FeC_3 component, which resulted in the encapsulated Fe nanoparticles. The energy dispersive spectrometer (EDS) mapping also revealed that the elements of C, N, and O were well dispersed in the FCM-800, while a low content of Fe nanoparticles was observed (**Fig. S1g**).

The comprehensive characterizations were carried out to analyze the prepared catalysts. The XRD patterns of FCM materials demonstrated that at comparably low carbonization temperatures (FCM-500 and FCM-600), only two broad diffraction peaks were observed at 24° and 43°, corresponding to the (002) lattice plane of graphitic carbon and the (101) plane of disordered carbon layers (Fig. 1f), respectively [43,44]. In contrast, FCMs prepared at comparably high temperatures (FCM-700 and FCM-800) exhibited four distinct iron-containing phases, such as weak signals for FeF_2, Fe_2O_3, Fe_3C, and metallic Fe^0, which was attributed to reactions between PVDF and $Fe(NO_3)_3{\cdot}9H_2O$ during carbonization: FeF_2 formed via fluorination (e.g., $CF_x + FeO_x \rightarrow FeF_2 + CO_2$) [45], while iron oxides were partially reduced by carbon to yield Fe^0 and Fe_3C. TGA analysis of FCMs was conducted (**Fig. S2**). FCM-500 displayed a mass loss starting at 400 °C [46], whereas FCM-800 exhibited degradation onset at 500 °C. At the final temperature (800 °C), FCM-500 and FCM-800 exhibited the mass losses of 95 % and 90 %, respectively, indicating that a certain content of Fe nanoparticles existed in FCMs. N_2 adsorption-desorption isotherms revealed that all FCMs exhibited Type IV isotherms (Fig. 1g), typical characteristics of mesoporous carbon materials [47,48]. The specific surface area (SSA) indicated a gradual decline alongside increasing carbonization temperature (Table 1). This trend aligned with higher temperatures promoting iron-catalyzed carbon dissolution/reprecipitation, which densified the carbon matrix and reduced the porosity [49]. Raman spectra display two prominent peaks,

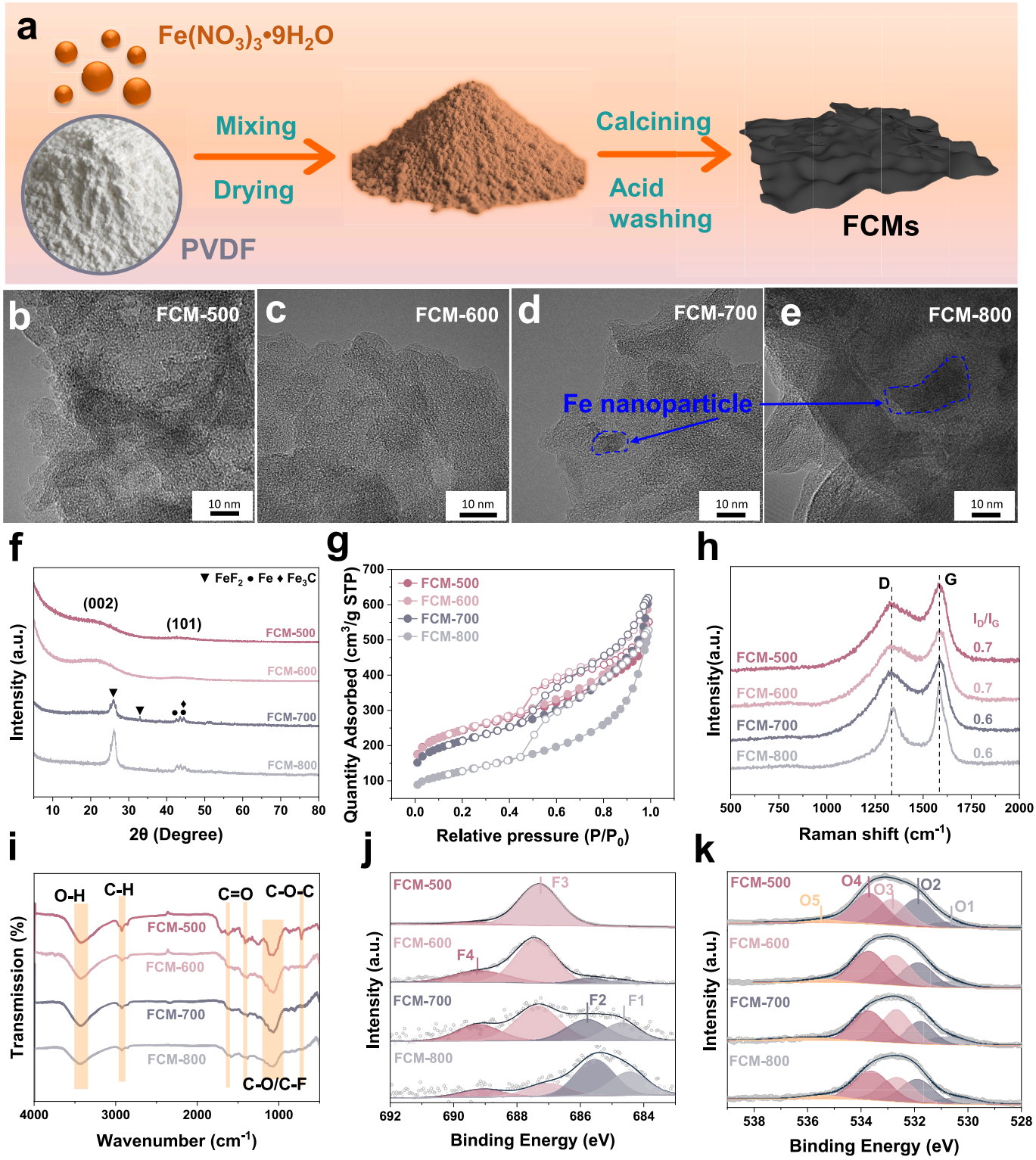

Fig. 1. (a) Schematic illustration of the preparation of FCMs materials. (b-e) HRTEM images, (f) XRD patterns, (g) N_2 adsorption/desorption isotherms, (h) Raman spectra, (i) FTIR spectra of FCMs materials. High-resolution deconvolution of F_{1s} (j) and O_{1s} (k) XPS spectra of FCMs.

the disorder-induced D-band in 1350 cm^{-1} and the graphitic G-band in 1590 cm^{-1} (Fig. 1h) [50]. The surface defects of FCMs contain edge carbons, oxygen functionalities, and F dopants, which are located at graphite carbon skeleton, edge carbon, or defect carbon atoms [51,52]. Herein, the increase of temperature from 500 to 800 °C would remove part of the F dopants on the carbon surface, leading to the decrease of the density of defects (I_D/I_G) on FCMs. FTIR spectra show the identified functional groups in FCMs (Fig. 1i). Peaks located at 1200 cm^{-1}, 1075 cm^{-1}, 1413 cm^{-1} and 1621 cm^{-1}, 2923 cm^{-1}, and 3423 cm^{-1} were corresponded to C—F bond, C—O group, C—H bending, C═O (carbonyl) stretching vibrations, C—H stretching, and O—H group [53–55], suggesting the existence of the hydrofluorocarbon and oxidized moieties [56].

XPS analysis confirms the presence of F and O on all FCM surfaces

Table 1
Physical/chemical properties of FCMs and their catalytic performance. [a]

Catalyst	SSA[b] (m^2 g^{-1})	I_D/I_G [c]	*E*. [d] ($\times10^{-1}$ at. %)		Deconvolution of F_{1s}[d] ($\times10^{-1}$ at.%)				Deconvolution of O_{1s}[d] ($\times10^{-1}$ at.%)				R_g[e] (mmol min^{-1} g^{-1})	R_m[f] ($\times10^{-2}$ mmol min^{-1} m^{-2})	Con. (%)	Sel. (%)	Ref.
			F_{1s}	O_{1s}	F1	F2	F3	F4	O1	O2	O3	O4					
Blank	–	–	–	–	–	–	–	–	–	–	–	–	–	–	35.8	90.5	
FCM-500	825.0	0.7	58.2	64.6	0	0	57.8	0.4	4.9	14.4	17.1	26.4	5.4	0.7	94.5 ± 2.5	>99	
FCM-600	833.5	0.7	9.8	62.2	0.4	0.7	6.4	2.3	4.1	12.3	19.1	23.5	5.1	0.6	88.5 ± 1.6	>99	
FCM-700	734.4	0.6	4.9	42.7	0.8	1.1	2	1	3.9	8.6	13.8	14.2	4.2	0.6	81.7 ± 1.8	>99	
FCM-800	446.0	0.6	2.4	31.1	1	0.8	0.3	0.3	2.9	6.4	10.2	10.4	4.0	0.9	78.2 ± 3.8	>99	
Fe-FCM-800	–	–	–	–	–	–	–	–	–	–	–	–	3.4	–	75.6 ± 2.9	98 ± 1.2	
NSC-773	57	–	–	44	–	–	–	–	–	–	–	–	2.5	4.4	95.0	98	[60]
MA500	635	–	–	0.1	–	–	–	–	–	–	–	–	0.6	0.1	88.0	>99	[61]

[a]Conditions: 400 mg catalyst, 170 mmol BO, 7.1 mmol TBAB, 10 mmol DCB, 1.0 MPa CO_2, 110 °C, 1100 rpm, 4 h. [b] Specific surface area. [c] Date from Raman spectra. [d] Date from XPS spectra (F1, F2, F3, and F4 represent FeF_2, ionic C—F, semi-ionic C—F, and covalent C—F, respectively; O1, O2, O3, and O4 represent carbonyl/quinone carbonyl, carboxyl, C–O–C, and –OH, respectively). [e] The initial rate normalized by the catalyst mass with the BO conversion <20 %. [f] The initial rate normalized by the specific surface area with the BO conversion <20 %.

(**Fig. S3a**), originating from C—F bonds in PVDF during the carbonization process. As the temperature increased, the F content decreased from 5.8 at.% (FCM-500) to 0.2 at.% (FCM-800), while the content of oxygen element declined from 6.5 at.% to 3.1 at.%, reflecting the thermal removal of less stable fluorinated and oxygenated species [57]. The high-resolution deconvolution F_{1s} XPS spectra of FCMs was conducted (Fig. 1j), revealing four distinct components, including FeF_2 (F1, 684.7 ± 0.1 eV), ionic C—F bonds (F2, 685.8 ± 0.1 eV), semi-ionic C—F bonds (F3, 687.3 ± 0.1 eV), and covalent C—F bonds (F4, 689.2 ± 0.1 eV) [45]. For FCM-500, only F3 and F4 species were detected, and F3 was the predominant component. However, as the carbonization temperature increased, the relative content of F3 progressively decreased due to its thermal instability, while the contributions of F2 and F1 increased. This trend aligns with the XRD observations regarding iron speciation (e.g., the formation of FeF_2). In Fig. 1k, the high-resolution deconvolution O_{1s} XPS spectra was conducted, and five peaks, including carbonyl/quinone groups O1 (O1, 530.9 ± 0.1 eV), carboxylic groups (O2, 531.8 ± 0.1 eV), ether groups (C–O–C) (O3, 532.7 ± 0.1 eV) and hydroxyl groups (–OH) (O4, 533.6 ± 0.1 eV) and physiosorbed O_2 (O5, 535.7 ± 0.2 eV) [58,59], were obtained. The O2, O3, and O4 groups dominated the surface functionalities across all the samples. Also, with rising carbonization temperature, the relative content of the O4 group slightly decreased, whereas the content of the O3 group exhibited a minor increase. Notably, the contributions of the O1 and O2 groups remained almost unchanged. These results were consistent with the FTIR analysis. Additionally, the XPS analysis results demonstrated that there was no Fe species on the surface of FCMs, indicating that the Fe nanoparticles were totally encapsulated by the carbon layers (**Fig. S3b**).

The catalytic performances of FCMs in the CO_2 cycloaddition are summarized in Table 1. We find that the catalytic performance of the carbon materials gradually increases with decreasing carbonization temperature. FCM-500 exhibits the best catalytic activity for CO_2 cycloaddition, achieving 94 % BO conversion with a high mass-normalized initial reaction rate (R_g, 5.4 mmol g_{Cat}^{-1} min^{-1}), better than other FCMs (79.6 % ~ 89.8 % conversion, 4.0–5.1 mmol g_{Cat}^{-1} min^{-1}). This activity also is competitive to the state of art catalysts, such as N-doped carbon (0.6 mmol g_{Cat}^{-1} min^{-1} for N-doped active carbon (MA500), 2.7 mmol g_{Cat}^{-1} min^{-1} for N-doped carbon/ZnO hybrid material (Zn-Asp-300), 3.8 mmol g_{Cat}^{-1} min^{-1} for urea-glucose carbonaceous material (U-GCM)) and S, N co-doped carbon (2.5 mmol g_{Cat}^{-1} min^{-1} for NSC-773), and other metal based carbon materials [60–63], etc. (Table 1 and **Table S1**). Pseudo-first-order kinetic fittings for FCM-500 and FCM-800 were carried out and revealed that the rate constants (*k*) of 0.6 h^{-1} for FCM-500 and 0.3 h^{-1} for FCM-800 were obtained (Fig. 2a), showing that the reaction could be facilitated by FCM-500. The apparent activation energies (E_a) for FCM-500 and FCM-800 were calculated to be 36.7 kJ mol^{-1} and 39.6 kJ mol^{-1} (Fig. 2b), which were lower than that of the blank experiment (42.0 kJ mol^{-1}), demonstrating that the presence of the FCMs would greatly lower the reaction barrier in the CO_2 cycloaddition. Meanwhile, $k_{FCM\text{-}500}$ (0.6 h^{-1}) was much higher than that of $k_{FCM\text{-}800}$ (0.3 h^{-1}), probably ascribed to the increased contents of F dopant and oxygen-containing groups, synergistically enhancing the catalytic activity. Moreover, it was observed that $E_{a,\ Blank}$ was 42.0 kJ mol^{-1}, demonstrating that this reaction process could be facilitated by adding more TBAB, which was not conducive to the economy and separation of the reaction. It might be argued that the existence of encapsulated iron particles would influence the catalytic performance of FCMs. Here, Fe-FCM-800 without acid-washing (**Fig. S2** and **S4**) was used as the catalyst for the CO_2 cycloaddition, displaying a 76.8 % BO conversion with an R_g of 3.5 mmol g_{Cat}^{-1} min^{-1}, slightly lower than FCM-800, confirming that residual iron particles did not significantly contribute to catalytic activity.

The recyclability of the catalyst is the key parameter for its industrial application. In this work, FCM-500 was used as the carbon catalyst for the cycling stability tests with 5 runs. The result demonstrated a slight decline in activity over FCM-500 for the CO_2 cycloaddition after the first cycle, followed by a stabilized activity in subsequent cycles (Fig. 3a). The characterization of recycled FCM-500 (r-FCM-500) showed that the honeycomb-like porous structure was retained (**Fig. S5**), The XPS analysis revealed that the contents of F (5.6 at.%) and O (6.7 at.%) were not changed significantly (Fig. 3c), compared with the pristine one (5.8 at.% for F and 6.5 at.% for O) (Table 1). Meanwhile, the high-resolution deconvolution of F_{1s} and O_{1s} XPS spectra further confirmed no apparent changes in the surface property of r-FCM-500 (**Fig. 3d** and **e**), evidencing the high stability of F doping in FCM during the reaction. The SSA decreased from 825.0 m^2 g^{-1} to 618.1 m^2 g^{-1} (Fig. 3f), suggesting partial structural collapse or the inside pores were blocked, which might be the primary factor responsible for the decline in catalytic performance of FCM-500 in the CO_2 cycloaddition.

3.2. DFT calculation

The DFT simulations were employed to elucidate the intrinsic role of surface functional groups in FCMs during the CO_2 cycloaddition reaction. Based on the proposed mechanism of metal-free carbon materials catalyzing CO_2 cycloaddition and prior studies, the ring-opening

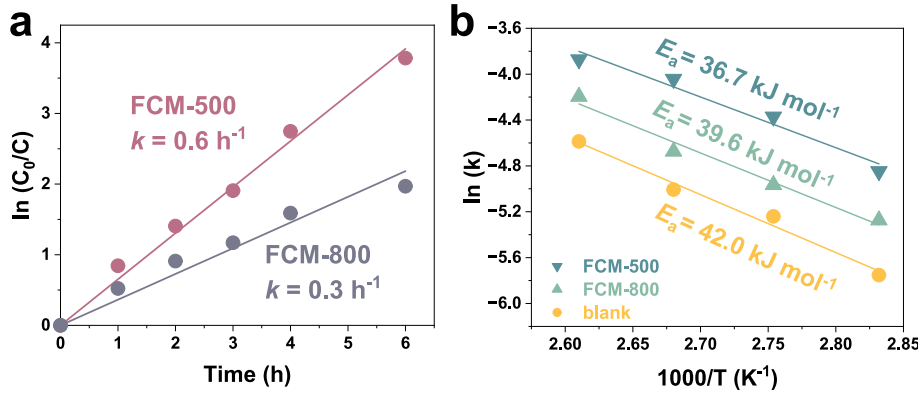

Fig. 2. (a) Pseudo first-order and (b) Arrhenius plots of CO_2 cycloaddition catalyzed by FCM-500 and FCM-800. Reaction conditions: 170 mmol BO, 7.1 mmol TBAB, 10 mmol DCB, 400 mg catalysts, 1.0 Mpa CO_2, 1100 rpm, 110 °C.

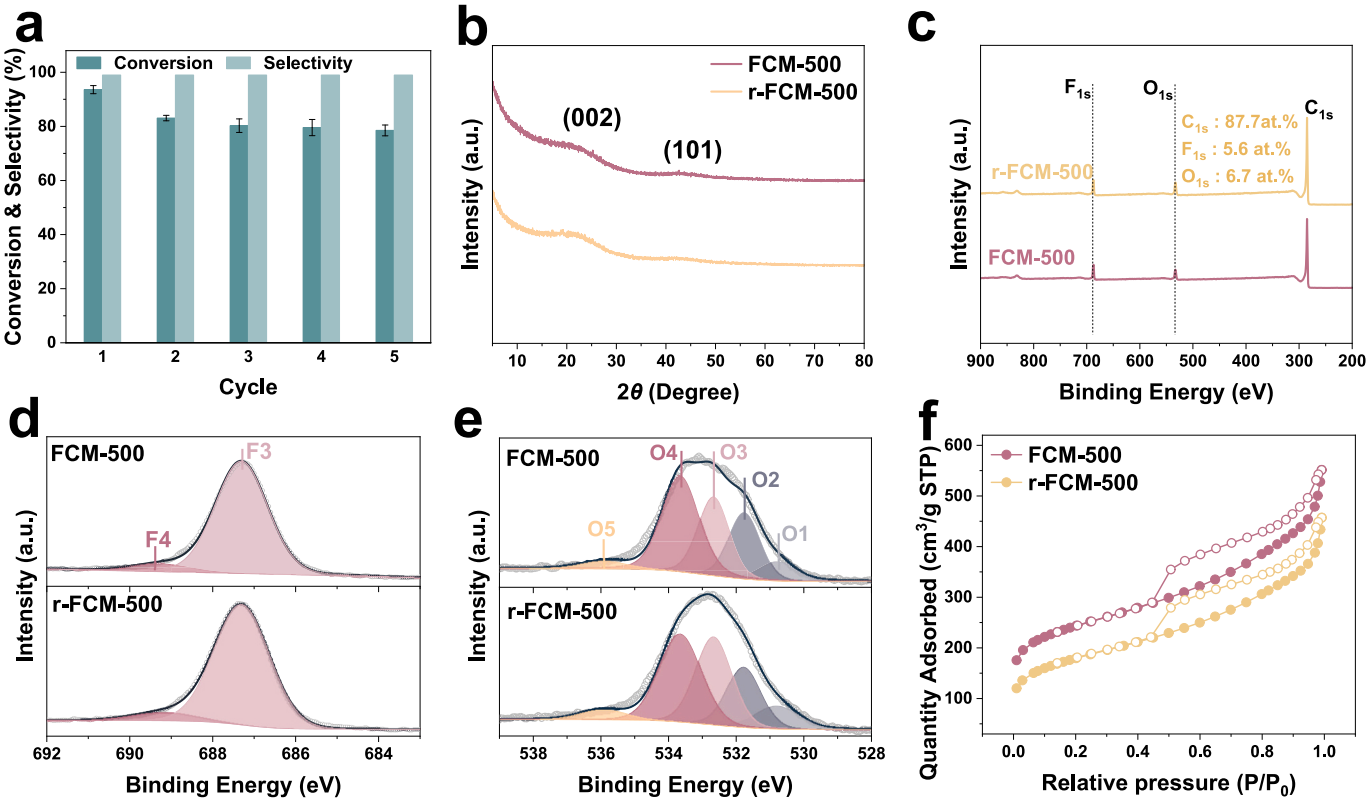

Fig. 3. (a) Stability test of FCM-500. Reaction conditions: 170 mmol BO, 7.1 mmol TBAB, 10 mmol DCB, 400 mg catalysts, 1.0 MPa CO_2, 1100 rpm, 110 °C, 4 h. (b) XRD patterns, and (c) XPS survey of the pristine and used catalysts. High-resolution deconvolution of F_{1s} (d) and O_{1s} (e) XPS spectra of r-FCM-500. (f) N_2 adsorption-desorption isotherms of the pristine and used catalysts.

reaction of BO to form the transient alkoxide intermediate C_4H_8OBr (Int.1) was identified as a critical step in the reaction [60,64]. The characterizations confirmed that F and O species dominated the surface of FCMs and enhanced the CO_2 cycloaddition with BO. The –OH groups act as hydrogen-bond donors, modulating the electron cloud distribution of BO via hydrogen bonding with its oxygen atom, thereby facilitating the ring-opening reaction [65]. To elucidate this mechanism, six kinds of catalyst models were established: pristine graphite carbon (C1), carbon with isolated C—F bonds (C2), carbon with isolated –OH groups (C3), carbon co-functionalized with both C—F, and –OH (C4), encapsulated iron by graphite (C5), and encapsulated iron by F-doped carbon (C6), which served as the adsorbents for the adsorption simulations (**Table S2**).

DFT-optimized adsorption models and their corresponding adsorption energies (E_{ads}) are summarized in Fig. 4a. For the adsorption of BO, the value of $E_{ads,\ C1}$ was calculated to be −0.3 eV. When F and O elements were introduced, the value of $E_{ads,\ C2}$ and $E_{ads,\ C3}$ were calculated to be −0.4 eV and − 0.9 eV, respectively, suggesting that localized electronic redistribution induced by F doping or O functionality would enhance the BO adsorption [66,67]. While, the OH-functionalized carbon was found to be more favorable to adsorb BO on the surface [68,69]. Remarkably, the co-existence of C—F and –OH groups in C4 further improved E_{ads} to −1.0 eV. This highlighted a synergistic effect between adjacent C—F and –OH groups, where F doping amplified the hydrogen-bond-mediated adsorption capability of –OH, thereby facilitating the catalytic performance. This result also demonstrated that the role of F dopants in this work might be similar to that of N dopants, which could efficiently interact with BO and CO_2 molecules to facilitate the reaction

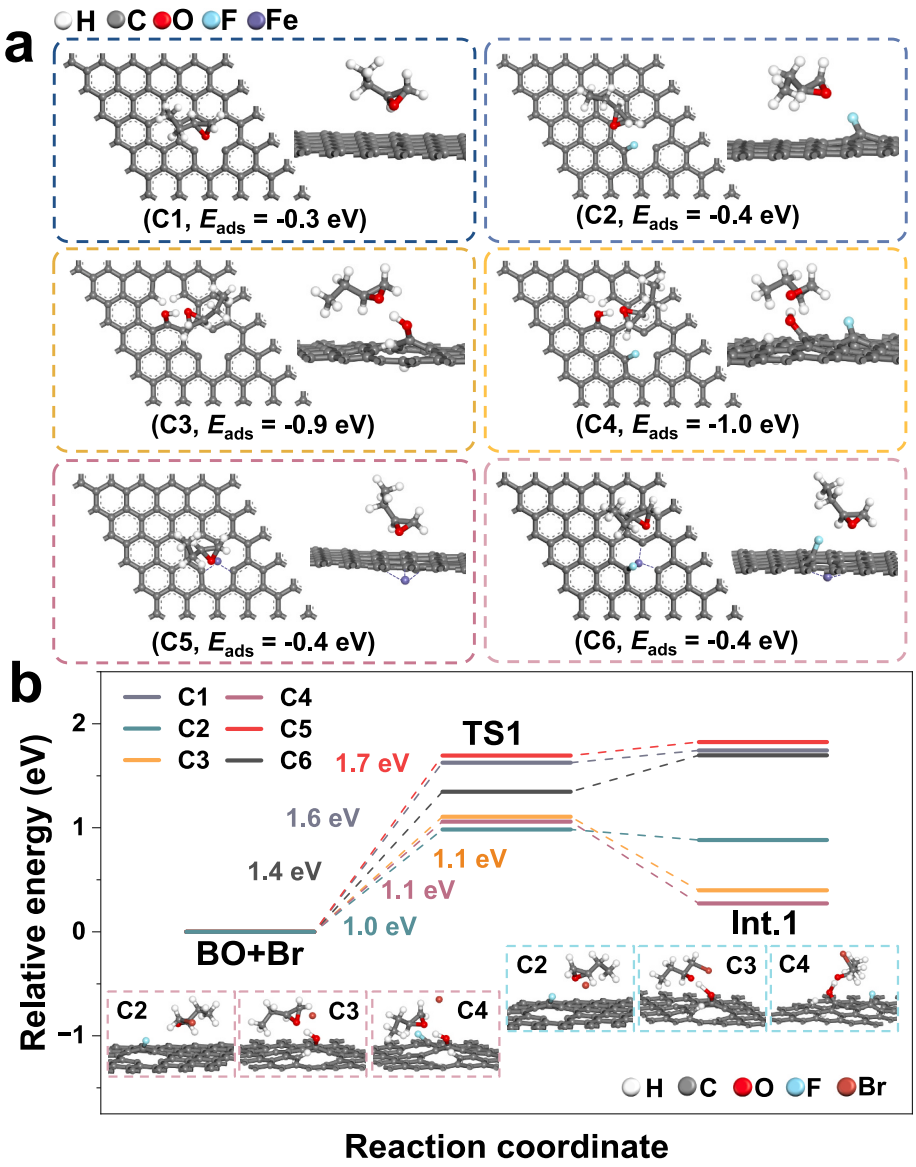

Fig. 4. (a) Structure optimization of BO and carbon adsorbent from the DFT calculation, and (b) energy barrier of ring-opening reaction of BO to form Int.1.

[70]. Also, we believe that the F dopant displayed a higher electronegativity than that of the N dopant, which was probably favorable for the reaction. It was notable that the presence of Fe in the system (both $E_{ads,\ C5}$ and $E_{ads,\ C6}$) was calculated to be −0.4 eV, close to the $E_{ads,\ C2}$, showing the ignorable influence of Fe nanoparticles in this reaction, which agreed with the experiment results.

The energy barrier for the ring-opening of BO, a pivotal intermediate reaction step due to its inherent thermodynamic challenge [71], was further investigated via transition state (TS) calculations across all the catalyst models (Fig. 4b and **Table S3**). For the C1, the energy barrier for BO ring-opening (TS1) was 1.6 eV. For the C5, this barrier slightly increased to 1.7 eV, aligning with C1 and indicating negligible catalytic activity from Fe encapsulation alone. In contrast, the C6 reduced the barrier to 1.4 eV, demonstrating that F doping enhanced electronic modulation to facilitate the reaction. Strikingly, OH-functionalized models (1.1 eV for C3 and C4) exhibited a 0.6 eV reduction in the barrier compared to C1, attributed to hydrogen-bond-driven electron redistribution within BO, which weakened its intramolecular bonding and stabilized the transition state [72,73]. A synergistic effect emerged in C4: introducing fluorine adjacent to –OH groups marginally enhanced catalytic activity, lowering the barrier than that of C3. This aligned with the earlier adsorption trend (−1.0 eV for C4, −0.9 eV for C3), suggesting that C—F groups amplified the hydrogen-bonding capability of –OH. Notably, the F-doped model (C2) achieved the lowest forward barrier (1.0 eV), likely due to F doping-induced strong positive charges on adjacent carbons, producing Lewis acid sites with localized electron density, a distinct mechanism from traditional oxygen-based acidic groups [66]. However, the limited adsorption capacity (C2, E_{ads} = −0.4 eV) and the low reverse energy barrier of F doping hindered the catalytic efficiency. This contrasted with that of the OH-functionalized systems, where robust adsorption (C3, E_{ads} = −0.9 eV) ensured the enhanced substrate-catalyst interaction, even with slightly higher forward barriers. Overall, F doping modestly complemented hydroxyl groups in optimizing catalytic pathways, but its independent role remained constrained by weak adsorption and unfavorable thermodynamic reversibility.

3.3. *Structure-activity relationship*

To explore the structure-activity relationship, the intrinsic relationship between the physicochemical properties of FCMs and their corresponding catalytic activity was investigated. The SSA of carbon

materials is one of the crucial factors influencing their catalytic activity [74,75]. As shown in Fig. 5a, there was a positive correlation between the increase in the SSA of FCMs and the reaction rate (R_g). It can be concluded that as the specific surface area expanded, the number of exposed active sites on FCMs increased. Additionally, the content of active sites on the FCMs' surface was another significant factor affecting their catalytic performance. F atoms are typically doped at the edge positions of the carbon skeleton [76], which would benefit the surface defects of carbon materials. Therefore, the relationship between the defect degree (I_D/I_G ratio) of FCMs and R_g was investigated, and we found that the high defect density of FCMs indeed enhances the activity (R_g ranged from 4.0 to 5.4) (Fig. 5b). It was believed that the defect density on the carbon surface was greatly influenced by the content of F dopants and oxygen-containing groups, which were responsible for the catalytic activity of FCMs in the CO_2 cycloaddition reaction. Herein, the higher content of F dopants and oxygen-containing groups would increase the defect density, leading to the higher activity. Since the F doping would cause more defects on the carbon surface, the impact of the content of F dopants on R_g was further explored. As shown in **Fig. 5c,** F content in FCMs was positively correlated with R_g, with R_g increasing as F content rose. Further investigation into different F-containing functional groups revealed that the relative content of semi-ionic C—F bonds (F3) exhibited a positive correlation with R_g (Fig. 5d). Meanwhile, FeF_2 (F1), ionic C—F bonds (F2), and covalent C—F bonds (F4) showed a chaotic relationship with R_g (**Fig. S6a-c**).

Based on the reported literature, the oxygen-containing functional groups on carbon materials, such as carbonyl groups, carboxylic groups, and –OH groups, demonstrated beneficial effects on catalytic activity for CO_2 cycloaddition reactions [69,72]. Consequently, we systematically investigated the relationship between surface oxygen content, oxygen functional groups on FCMs, and R_g. As illustrated in **Fig. S6d-h**, no apparent correlation was observed between total surface oxygen content and R_g while carbonyl/quinone groups (O1), carboxylic groups (O2), and –OH groups (O4). There was also no apparent relationship between R_g and different ratios of F or O functionalities normalized by the SSA of FCMs (**Fig. S7**). These results demonstrated that the single functionality could not apparently enhance the reaction.

According to the aforementioned findings, we believed that O1, O2, O4, and F3 species on FCM surfaces served as active sites for CO_2 cycloaddition. To elucidate the intrinsic effects of these critical active sites, we established correlations between the R_g and the surface functional group content. The R_g values initially increased rapidly, then plateaued as the combined (O_{1s} + F_{1s}) content rose from 2.00 to 10.34 (Fig. 5e). A well-fitting was achieved when considering O1, O2, O4, and F3 concentrations collectively (Fig. 5f), indicating the synergistic effect of O1, O2, O4, and F3 on the catalytic activity for CO_2 cycloaddition. Given the strong correlation between FCMs' catalytic performance and their specific surface area (SSA), the areal site density was obtained by normalized surface active site concentrations (X/SSA). Subsequent analysis revealed that the pronounced linear positive correlations between R_g and both (O_{1s} + F_{1s})/SSA as well as (O1 + O2 + O4 + F3)/SSA (**Fig. 5g** and **h**), demonstrating that the areal density of fluorinated/oxygenated functionalities directly governed catalytic efficiency in the CO_2 cycloaddition with BO.

3.4. Kinetic study

In this work, kinetic experiments were performed by establishing substrate concentration gradients to determine corresponding reaction orders, with the rational control of CO_2 conversion below 20 % in each trial to ensure operation within the kinetic regime. Reaction quenching and product analysis were implemented immediately upon completion.

Based on the chemical reaction equations (Fig. 6), we proposed a reaction rate equation for the CO_2 cycloaddition (Eq. 2)

$$r = -k_0[BO]^{n_{BO}}[CO_2]^{n_{CO_2}}[TBAB]^{n_{TBAB}}[FCM]^{n_{FCM}} \quad (2)$$

n_{BO}, n_{TBAB}, and n_{FCM} represented the reaction order of BO, TBAB, and FCM-500, respectively, and were determined by the control variable method. k_0 was the reaction rate constant in $mol^{(1-n)}\,L^{(n-1)}\,min^{-1}$. [FCM] referred to the concentration of the exposed active site on the surface of FCM-500 in the reaction system. By substituting the results of SSA and XPS analysis of FCM-500 into **Eqs. S2-S6**, the contents of each fluorine and oxygen species exposed on the surface of FCM-500 and FCM-800 per unit mass were obtained (**Table S4**).

During the entire reaction, CO_2 was continuously charged to maintain the pressure of the reaction system. Therefore, the effect of CO_2

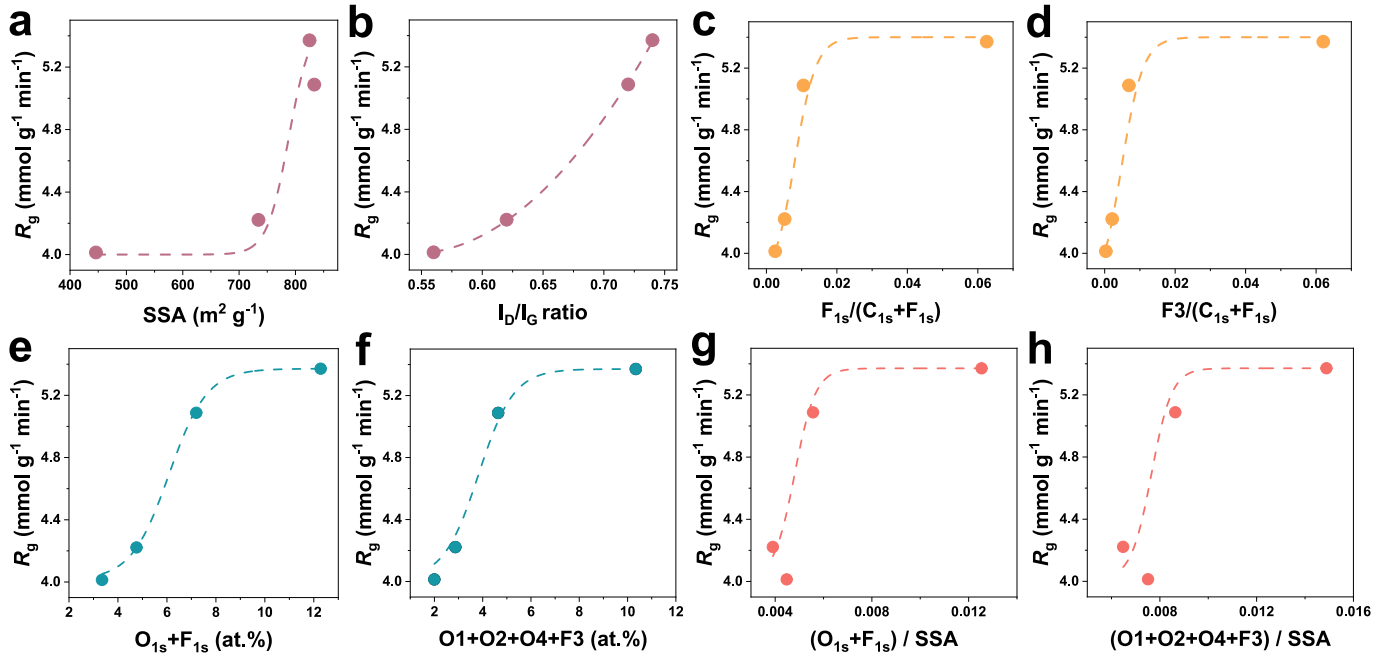

Fig. 5. Dependence of R_g on the SSA (a), defect degree (b), the amounts of gross F_{1s} content (c), the semi-ionic C—F bonding (d), O_{1s} + F_{1s} (e), O1 + O2 + O4 + F3 (f), (O_{1s} + F_{1s})/SSA (g), and (O1 + O2 + O4 + F3)/SSA (h) of FCMs.

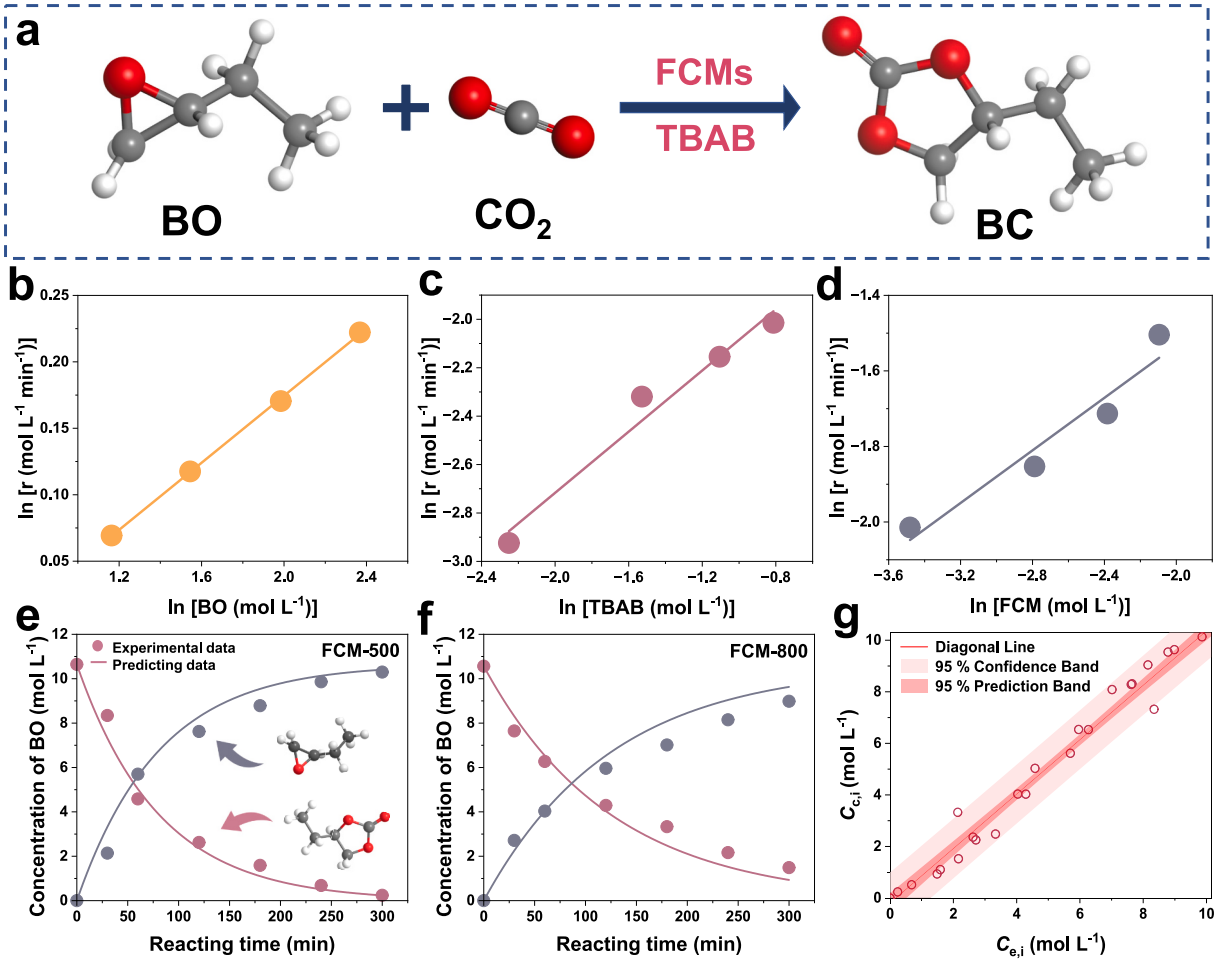

Fig. 6. (a) Schematic illustration of the cycloaddition reaction catalyzed by FCMs. Relationships between Ln *r* and BO (b), TBAB (c), and FCM-500 (d). Empirical and predicted values based on the kinetic model of FCM-500 (e) and FCM-800 (f). Reaction conditions: 170 mmol BO, 7.1 mmol TBAB, 10 mmol DCB, 400 mg catalysts, 1.0 Mpa CO_2, 1100 rpm, 110 °C. (g) Comparison of all experimental values and predicted values from Fig. 6e-f.

concentration on the reaction can be ignored. Here, the reaction order of CO_2 was considered to be 0 ($n_{CO_2} = 0$). Therefore, Eq. 3 can be obtained.

$$r = -k_0[BO]^{n_{BO}}[TBAB]^{n_{TBAB}}[FCM]^{n_{FCM}} \quad (3)$$

The kinetic experiments in this study were performed by varying the concentration of different substrates (**Table S5**). The reaction cardinality of the reaction was determined using BO in a concentration ranging of 5.0 to 10.7 mol L^{-1}. The curve of ln[r] vs. ln[BO] showed (Fig. 6b) that the experimental data fit well, and the apparent reaction order of BO (n_{BO}) was calculated to be 1. The first-order reaction kinetics of BO was confirmed [68]. The reaction order of TBAB was studied when the concentration of TBAB was in the range of 0.1 to 0.4 mol L^{-1}, while other reaction conditions were unchanged. As expected, the reaction rate increased with increasing TBAB concentration (Fig. 6c), and a good fit was observed between ln[r] vs. ln[BO]. The reaction order of TBAB (n_{TBAB}) was obtained (0.6). Based on the structure-activity relationship between FCMs and CO_2 cycloaddition reaction and the DFT calculation, the semi-ionic C—F bond and oxygen functional group on the surface of FCM-500 displayed considerable catalytic activity in the reaction. Therefore, the [FCM] term was the sum of the concentrations of F3, O1, O2, and O4 on the surface of FCM-500 in the system. The reaction order of [FCM] was explored by varying the dosage of FCM-500. The reaction rate increased with increasing concentration of FCM-500 (Fig. 6d), and ln[r] showed a good fit to ln[FCM]. The reaction order of FCM-500 (n_{FCM}) was calculated to be 0.4. Herein, the k_0 value was calculated to be 4.3 × 10^{-2} $mol^{-0.9}$ $L^{0.9}$ min^{-1}. Therefore, the kinetic model of the cycloaddition reaction of CO_2 and BO catalyzed by FCM-500 as a catalyst was summarized in **Eq. 4**.

$$r = -4.3 \times 10^{-2} \times [BO]^{1}[TBAB]^{0.6}[FCM]^{0.4} \quad (4)$$

To verify the feasibility of the obtained kinetic model of the FCMs-catalyzed system, we used this kinetic model to predict the concentrations of different substrates, which was conducted under different initial reaction conditions catalyzed by the carbon catalysts (Fig. 6e-f and **Table S6**). The results demonstrated that the predicted values were well-fitted with the experimental values, evidencing the predictability of the established kinetic model in this work.

The decisive exponent (ρ^2), F-test, and residual analysis (R^2) (Eqs. 5–7) were tested between the actual experimental and simulated calculated values to confirm the reliability of the kinetic model. It was observed that the value of ρ^2 was calculated to be 0.99. F_c was 216.4, which was higher than $F_{0.05}$ (9.55 under the current condition). And R^2 was 0.97. At the same time, the involved predicted and experimental values were also evenly distributed within the 95 % confidence intervals on both sides of the diagonal fitting line (Fig. 6f). These results further confirm that the established model in this work could well predict the catalytic properties of various F-doped metal-free carbon catalysts in the CO_2 cycloaddition.

$$\rho^2 = 1 - \frac{\sum_1^n (C_{e,i} - C_{c,i})^2}{\sum_1^n C_{e,i}^2} \quad (5)$$

$$F_c = \frac{\left[\sum_1^n C_{e,i}^2 - \sum_1^n \left(C_{e,i} - C_{c,i}\right)^2\right] / P}{\sum_1^n \left(C_{e,i} - C_{c,i}\right)^2 / n - p} \quad (6)$$

$$R^2 = \frac{\sum_1^n \left(C_{e,i} - C_{ave,i}\right)^2 - \sum_1^n \left(C_{e,i} - C_{c,i}\right)^2}{\sum_1^n \left(C_{e,i} - C_{ave,i}\right)^2} \quad (7)$$

where $C_{e,i}$ was the experimental value of the substance concentration in the system, $C_{c,i}$ was the calculated value of the substance concentration in the reaction system, $C_{ave,i}$ was the average of the experimental values of the reaction substance, P and n were the number of parameters and the number of experiments, respectively.

4. Conclusions

In summary, fluorine-doped carbon materials (FMCs) with fluorine and oxygen dual sites on the surface were fabricated through the one-step pyrolysis process, and the synergistic effect of both sites on the carbon dioxide (CO_2) cycloaddition was observed, which was confirmed by the density functional theory (DFT) simulations, structure-activity analysis, and kinetic elucidation. It was observed that the content of F and O showed a significant influence on the promotion of CO_2 cycloaddition, in which FCM synthesized at 500 °C (FCM-500) with 5.8 at.% F and 6.5 at.% O displayed the highest activity of 93.6 % yield with 5.4 mmol g_{Cat}^{-1} min^{-1} and 0.7×10^{-2} mmol m^{-2} min^{-1}. In this process, FCM-500 (36.7 kJ mol^{-1}) displayed a slightly lower activation energy than that of FCM synthesized at 800 °C (FCM-800) (39.6 kJ mol^{-1}), and $k_{FCM\text{-}500}$ (0.6 h^{-1}) was much higher than that of $k_{FCM\text{-}800}$ (0.3 h^{-1}). Here, we hypothesized that these results were probably a result of the synergistic effect of certain F species and oxygen-containing groups [34,77]. The DFT simulations and the structure-activity analysis of FCM materials revealed that the catalytic activity was highly related to oxygen species on the carbon surface and semi-ionic C—F bond. Therefore, a reliable kinetic model based on the surface functionalities was established, which was verified by well-predicting the concentration variation of substrates. This work paves a new insight into the F-doped nanocarbon as catalysts for the CO_2 cycloaddition, which was helpful to understand the reaction mechanism from the kinetic analysis as well.

CRediT authorship contribution statement

Jianhan Yang: Writing – original draft, Methodology, Investigation, Data curation. **Jiangnan Huang:** Writing – review & editing, Resources, Methodology, Investigation. **Hao-Fan Wang:** Validation, Resources, Methodology. **Hongjuan Wang:** Resources, Methodology. **Hao Yu:** Resources, Methodology. **Yonghai Cao:** Writing – review & editing, Validation, Supervision, Resources, Project administration.

Declaration of competing interest

The authors declare that they have no known competing financial interests or personal relationships that could have appeared to influence the work reported in this paper.

Acknowledgements

We would like to acknowledge the financial support from the National Natural Science Foundation of China (22272056), Guangdong Basic and Applied Basic Research Foundation (2022A1515140108), CNPC Innovation Found (no. 2021DQ02-0704), Research Fund Program of Guangdong Provincial Key Laboratory of Fuel Cell Technology (FC202305), and the start-up fund from Zhongkai College of Agricultural Engineering.

Appendix A. Supplementary data

Supplementary data to this article can be found online at https://doi.org/10.1016/j.jcis.2025.138922.

Data availability

Data will be made available on request.

References

[1] D. Zhou, E.S. Obobisa, E.C. Ayamba, Achieving carbon neutrality goal in European countries: the role of green technology innovation, renewable energy, and financial development, Environ. Dev. Sustain. (2024), https://doi.org/10.1007/s10668-10024-04989-10665.
[2] F. Kong, Y. Wang, How to understand carbon neutrality in the context of climate change? With special reference to China, Sustain. Environ. 8 (2022) 2062824.
[3] M. Shahbaz, A. Barut, H. Alofaysan, S. Çamkaya, The impact of inclusive finance and lifelong learning on carbon neutrality: evidence from African countries, Res. Int. Bus. Financ. 78 (2025) 102996.
[4] H. Zhong, Y. Su, X. Chen, X. Li, R. Wang, Imidazolium- and Triazine-based porous organic polymers for heterogeneous catalytic conversion of CO_2 into cyclic carbonates, ChemSusChem 10 (2017) 4855–4863.
[5] C. Cui, R. Sa, Z. Hong, H. Zhong, R. Wang, Ionic-liquid-modified click-based porous organic polymers for controlling capture and catalytic conversion of CO2, ChemSusChem 13 (2020) 180–187.
[6] H. Wang, Y. Shao, S. Mei, Y. Lu, M. Zhang, J.-K. Sun, K. Matyjaszewski, M. Antonietti, J. Yuan, Polymer-derived heteroatom-doped porous carbon materials, Chem. Rev. 120 (2020) 9363–9419.
[7] S. Yu, J. He, Z. Zhang, Z. Sun, M. Xie, Y. Xu, X. Bie, Q. Li, Y. Zhang, M. Sevilla, M.-M. Titirici, H. Zhou, Towards negative emissions: hydrothermal carbonization of biomass for sustainable carbon materials, Adv. Mater. 36 (2024) 2307412.
[8] E. Lepre, S. Rat, C. Cavedon, P.H. Seeberger, B. Pieber, M. Antonietti, N. Lopez-Salas, Catalytic properties of high nitrogen content carbonaceous materials, Angew. Chem. Int. Ed. 62 (2022) e202211663.
[9] Y.-X. Liu, H.-H. Wang, T.-J. Zhao, B. Zhang, H. Su, Z.-H. Xue, X.-H. Li, J.-S. Chen, Schottky barrier induced coupled Interface of Electron-rich N-doped carbon and Electron-deficient cu: in-built Lewis Acid-Base pairs for highly efficient CO_2 fixation, J. Am. Chem. Soc. 141 (2019) 38–41.
[10] Q. Yang, C.-C. Yang, C.-H. Lin, H.-L. Jiang, Metal-organic-framework-derived hollow N-doped porous carbon with ultrahigh concentrations of single Zn atoms for efficient carbon dioxide conversion, Angew. Chem. Int. Ed. 58 (2019) 3511–3515.
[11] D.S. Su, S. Perathoner, G. Centi, Nanocarbons for the development of advanced catalysts, Chem. Rev. 113 (2013) 5782–5816.
[12] Y. Cao, S. Mao, M. Li, Y. Chen, Y. Wang, Metal/porous carbon composites for heterogeneous catalysis: old catalysts with improved performance promoted by N-doping, ACS Catal. (2017) 8090–8112.
[13] D.S. Su, G. Wen, S. Wu, F. Peng, R. Schlogl, Carbocatalysis in liquid-phase reactions, Angew. Chem. Int. Ed. 56 (2017) 936–964.
[14] Z.W. Liu, F. Peng, H.J. Wang, H. Yu, W.X. Zheng, J.A. Yang, Phosphorus-doped graphite layers with high electrocatalytic activity for the O_2 reduction in an alkaline medium, Angew. Chem. Int. Ed. 50 (2011) 3257–3261.
[15] H. Yu, F. Peng, J. Tan, X. Hu, H. Wang, J. Yang, W. Zheng, Selective catalysis of the aerobic oxidation of cyclohexane in the liquid phase by carbon nanotubes, Angew. Chem. Int. Ed. 50 (2011) 3978–3982.
[16] Y. Cao, H. Yu, F. Peng, H. Wang, Selective allylic oxidation of cyclohexene catalyzed by nitrogen-doped carbon nanotubes, ACS Catal. 4 (2014) 1617–1625.
[17] H. Fu, K. Huang, G. Yang, Y. Cao, H. Wang, F. Peng, X. Cai, H. Gao, Y. Liao, H. Yu, Understanding the catalytic sites in porous hexagonal boron nitride for the epoxidation of styrene, ACS Catal. 11 (2021) 8872–8880.
[18] H. Fu, K. Huang, G. Yang, Y. Cao, H. Wang, F. Peng, Q. Wang, H. Yu, Synergistic effect of nitrogen dopants on carbon nanotubes on the catalytic selective epoxidation of styrene, ACS Catal. 10 (2020) 129–137.
[19] Y.H. Cao, H. Yu, J. Tan, F. Peng, H.J. Wang, J. Li, W.X. Zheng, N.B. Wong, Nitrogen-, phosphorous- and boron-doped carbon nanotubes as catalysts for the aerobic oxidation of cyclohexane, Carbon 57 (2013) 433–442.
[20] C. Mu, Y. Cao, H. Wang, H. Yu, F. Peng, A kinetics study on cumene oxidation catalyzed by carbon nanotubes: effect of N-doping, Chem. Eng. Sci. 177 (2018) 391–398.
[21] Z. Cai, M. Yuan, H. Wang, H.-F. Wang, S. Li, Y. Cao, H. Yu, F. Peng, Elucidating the influence of N doping on production of ε-Caprolactone catalyzed by Nanocarbon: a kinetic model from batch to Semibatch and continuous-flow operations, Ind. Eng. Chem. Res. 64 (2025) 4845–4857.
[22] J. Albero, H. Garcia, Doped graphenes in catalysis, J. Mol. Catal. A Chem. 408 (2015) 296–309.
[23] X. Liu, L. Dai, Carbon-based metal-free catalysts, Nat. Rev. Mater. 1 (2016) 16064.
[24] X.-H. Li, M. Antonietti, Metal nanoparticles at mesoporous N-doped carbons and carbon nitrides: functional Mott-Schottky heterojunctions for catalysis, Chem. Soc. Rev. 42 (2013) 6593–6604.
[25] Q. Liu, S. Yang, Y. Liu, J. Liang, L. Chen, J. Liu, S. Liu, Y. Yang, Z. Yu, F-doped self-supporting carbon electrode to improve carbon-water reaction assisted electrolysis of water for hydrogen production, Fuel 375 (2024) 132512.

[26] D. Wang, L. Zhang, Y. Fu, Z. Sun, T. Wang, Y. Shi, G. Yang, R. Ma, Z. Liu, L. Wu, Q. Zhang, Y. Wu, D. He, Fluorine doping modulating pore structure and adsorption capability of carbon matrix boosting potassium storage performance of red phosphorus anode, Adv. Funct. Mater. 34 (2024).

[27] J. Liang, L. Liang, B. Zeng, B. Feng, L. Du, X. Qiu, Y. Wang, H. Song, S. Liao, M. Shao, Z. Cui, Fluorine-doped carbon support enables superfast oxygen reduction kinetics by breaking the scaling relationship, Angew. Chem. Int. Ed. 63 (2024) e202412825.

[28] X. Shao, A. Maibam, F. Cao, H. Jin, S. Huang, M. Liang, M. Gyu Kim, K. My Tran, A. R. Jadhav, H. Seung Jung, R. Babarao, H. Lee, Coordination environment and distance optimization of dual single atoms on fluorine-doped carbon nanotubes for chlorine evolution reaction, Angew. Chem. Int. Ed. 63 (2024) e202406273.

[29] J. Xie, X. Zhao, M. Wu, Q. Li, Y. Wang, J. Yao, Metal-free fluorine-doped carbon Electrocatalyst for CO2 reduction outcompeting hydrogen evolution, Angew. Chem. Int. Ed. 57 (2018) 9640–9644.

[30] J. Zhao, X. Tian, Q. Niu, P. Zhang, F-doped carbon derived from asphalt by mechanochemical approach: more effective toward selective CO2 capture, Sep. Purif. Technol. 332 (2024) 125760.

[31] D.L. Kane, B.C. Figula, K. Balaraman, J.A. Bertke, C. Wolf, Cryogenic Organometallic Carbon–Fluoride Bond Functionalization with Broad Functional Group Tolerance, J. Am. Chem. Soc. 147 (2025) 5764–5774.

[32] Z. Zhao, X. Bai, H. Zhu, W. Liu, Y. Qi, T. Li, Y. Bai, Promoting the Normal- and low-temperature performances of natural graphite by the F-doping derived from PVDF modification, ACS Appl. Electron. Mater. 4 (2022) 4936–4946.

[33] X. Tao, R. Lu, L. Ni, V. Gridin, S. Al-Hilfi, Z. Qiu, Y. Zhao, U. Kramm, Y. Zhou, K. Müllen, Facilitating the acidic oxygen reduction of Fe-N-C catalysts by fluorine-doping, Mater. Horiz. 9 (2022) 417–424.

[34] Y. Cao, J. Huang, X. Peng, D. Cao, A. Galaska, S. Qiu, J. Liu, M.A. Khan, D. P. Young, J.E. Ryu, H. Feng, N. Yerra, Z. Guo, Poly(vinylidene fluoride) derived fluorine-doped magnetic carbon nanoadsorbents for enhanced chromium removal, Carbon 115 (2017) 503–514.

[35] I. Pereira da Silva, A. Maged, V. Pinheiro Lima Abreu, A. Luisa Quintanilha Candido, S. Denise Ferreira Rocha, E. Coutinho de Paula, Transfiguration of discarded PVDF ultrafiltration membranes: optimization of pyrolysis parameters for high-value char production, Waste Manage. (Oxford) 190 (2024) 360–369.

[36] P. Slobodian, B. Hausnerova, P. Riha, V. Pata, R. Olejnik, J. Matyas, Turning plastic waste immiscibility into an advantage: efficiency improvement of PVDF-based energy harvesters using post-consumer thermoplastics, Adv. Mater. Interfaces 12 (2025) 2500070.

[37] P. Hohenberg, W. Kohn, Inhomogeneous Electron gas, Phys. Rev. 136 (1964) B864–B871.

[38] Blochl, Projector augmented-wave method, Phys. Rev. B: Condens. Matter 50 (1994) 17953–17979.

[39] B. Delley, From molecules to solids with the DMol3 approach, J. Chem. Phys. 113 (2000) 7756–7764.

[40] M. He, Y. Wang, X. Zhang, H. Zhang, Y. Meng, D. Shang, H. Xue, D. Li, Z. Wu, Stability of iron-containing nanoparticles for selectively growing single-walled carbon nanotubes, Carbon 158 (2020) 795–801.

[41] L.P. Ding, B. McLean, Z.W. Xu, X. Kong, D. Hedman, L. Qiu, A.J. Page, F. Ding, Why carbon nanotubes grow, J. Am. Chem. Soc. 144 (2022) 5606–5613.

[42] E. Leppanen, S. Sainio, H. Jiang, B. Mikladal, I. Varjos, T. Laurila, Effect of electrochemical oxidation on physicochemical properties of Fe-containing single-walled carbon nanotubes, ChemElectroChem 7 (2020) 4136–4143.

[43] D. Mallesh, J. Anbarasan, P. Kumar, K. Upendar, P. Chandrashekar, B. Rao, N. Linglan, Synthesis, characterization of carbon adsorbents derived from waste biomass and its application to CO_2 capture, Appl. Surf. Sci. 530 (2020) 147226.

[44] J. Serafin, B. Dziejarski, O.F.C. Junior, J. Srenscek-Nazzal, Design of highly microporous activated carbons based on walnut shell biomass for H_2 and CO_2 storage, Carbon 201 (2023) 633–647.

[45] Y. Cao, J. Huang, X. Peng, D. Cao, A. Galaska, S. Qiu, J. Liu, M. Khan, D. Young, J. Ryu, H. Feng, N. Yerra, Z. Guo, Poly(vinylidene fluoride) derived fluorine-doped magnetic carbon nanoadsorbents for enhanced chromium removal, Carbon 115 (2017) 503–514.

[46] D. Losic, F. Farivar, P. Yap, A. Karami, Accounting carbonaceous counterfeits in graphene materials using the thermogravimetric analysis (TGA) approach, Anal. Chem. 93 (2021) 11859–11867.

[47] G. Cruz, L. Kubonová, D. Aguirre, L. Matejová, P. Peikertová, I. Troppová, E. Cegmed, A. Wach, P. Kustrowski, M. Gomez, L. Obalová, Activated carbons prepared from a broad range of residual agricultural biomasses tested for xylene abatement in the GaS phase, ACS Sustain. Chem. Eng. 5 (2017) 2368–2374.

[48] G. Zhang, H. Luo, H. Li, L. Wang, B. Han, H. Zhang, Y. Li, Z. Chang, Y. Kuang, X. Sun, ZnO-promoted dechlorination for hierarchically nanoporous carbon as superior oxygen reduction electrocatalyst, Nano Energy 26 (2016) 241–247.

[49] Y. Xiao, L. Ding, A. Leghari, D. Hungwe, M. Gao, Y. Gao, Y. Zhang, X. Chen, F. Wang, Ferric sludge derived pyrolyzed-hydrochar supported iron catalysts for catalytic cracking of toluene, Chem. Eng. J. 491 (2024) 152001.

[50] D. Saikia, T. Wang, C. Chou, J. Fang, L. Tsai, H. Kao, A comparative study of ordered mesoporous carbons with different pore structures as anode materials for lithium-ion batteries, RSC Adv. 5 (2015) 42922–42930.

[51] R. Guo, X. Liu, B. Wen, F. Liu, J. Meng, P. Wu, J. Wu, Q. Li, L. Mai, Engineering mesoporous structure in amorphous carbon boosts potassium storage with high initial coulombic efficiency, Nano-Micro. Lett. 12 (2020) 148.

[52] F. Wang, L. Wang, Q. Xue, Fluorine and sulfur co-doped amorphous carbon films to achieve ultra-low friction under high vacuum, Carbon 96 (2016) 411–420.

[53] U. Kamran, K. Rhee, S. Lee, S. Park, Solvent-free conversion of cucumber peels to N-doped microporous carbons for efficient CO_2 capture performance, J. Clean. Prod. 369 (2022) 133367.

[54] C. Saka, A. Levent, High-performance pseudo-capacitance supercapacitor with highly mesoporous fluorine doped polymeric carbon nitride nanosheets as electrode material, Diamond Relat. Mater. 148 (2024) 111504.

[55] Y. Panahian, N. Arsalani, Synthesis of Hedgehoglike F-TiO_2(B)/CNT nanocomposites for Sonophotocatalytic and photocatalytic degradation of malachite green (MG) under visible light: kinetic study, J. Phys. Chem. A 121 (2017) 5614–5624.

[56] T. Ding, W. Xu, J. Zhang, X. Zhang, H. Sun, L. Shi, J. Wei, D. Xu, S. Zhang, X. Duan, J. Zhang, S. Wang, H. Sun, Green preparation of fiberboard waste derived N-doped carbon catalysts with tailored properties for efficient hydrogenation reduction of nitroaromatics, Chem. Eng. J. 489 (2024) 151197.

[57] A. Peng, S. Qi, X. Liu, D. Xue, S. Peng, G. Yu, X. Liu, L. Sun, N-doped porous carbons derived from a polymer precursor with a record-high N content: efficient adsorbents for CO_2 capture, Chem. Eng. J. 372 (2019) 656–664.

[58] M. Shafeeyan, W. Daud, A. Houshmand, A. Shamiri, A review on surface modification of activated carbon for carbon dioxide adsorption, J. Anal. Appl. Pyrol. 89 (2010) 143–151.

[59] Z. Cai, D. Liu, J. Huang, J. Feng, H. Wang, G. Yang, F. Peng, Y. Cao, H. Yu, Solvent-free production of ε-Caprolactone from oxidation of cyclohexanone catalyzed by nitrogen-doped carbon nanotubes, Ind. Eng. Chem. Res. 61 (2022) 2037–2044.

[60] A. Ghosh, G.N. Reddy, P.K.M. Siddhique, S. Chatterjee, S. Bhattacharjee, R. Maitra, S.E. Lyubimov, A.V. Arzumanyan, A. Naumkin, A. Bhaumik, B. Chowdhury, Fabrication of a hollow sphere N,S co-doped bifunctional carbon catalyst for sustainable fixation of CO_2 to cyclic carbonates, Green Chem. 24 (2022) 1673–1692.

[61] A. Samikannu, L.J. Konwar, P. Maki-Arvela, J.P. Mikkola, Renewable N-doped active carbons as efficient catalysts for direct synthesis of cyclic carbonates from epoxides and CO_2, Appl. Catal. B: Env. 241 (2019) 41–51.

[62] R.B. Mujmule, W.J. Chung, H. Kim, Chemical fixation of carbon dioxide catalyzed via hydroxyl and carboxyl-rich glucose carbonaceous material as a heterogeneous catalyst, Chem. Eng. J. 395 (2020) 125164.

[63] W.L. Dai, M.L. Zou, J.F. Long, B. Li, S.Q. Zhang, L.X. Yang, D. Wang, P. Mao, S. L. Luo, X.B. Luo, Nanoporous N-doped carbon/ZnO hybrid derived from zinc aspartate: an acid-base bifunctional catalyst for efficient fixation of carbon dioxide into cyclic carbonates, Appl. Surf. Sci. 540 (2021) 148311.

[64] H. Chand, P. Choudhary, A. Kumar, V. Krishnan, Atmospheric pressure conversion of carbon dioxide to cyclic carbonates using a metal-free Lewis acid-base bifunctional heterogeneous catalyst, J. CO2 Util. 51 (2021) 101646.

[65] Z. Yue, M. Pudukudy, S. Chen, Y. Liu, W. Zhao, J. Wang, S. Shan, Q. Jia, A non-metal Acen-H catalyst for the chemical fixation of CO_2 into cyclic carbonates under solvent- and halide-free mild reaction conditions, Appl. Catal. Gen. 601 (2020) 117646.

[66] Q. Song, F. Zhao, Q. Wang, B. Dai, A highly efficient Lewis acid catalyst of F-doped activated carbon for acetylene dimerization, Mol. Catal. 564 (2024) 114321.

[67] X. Chen, J. Xiao, J. Wang, D. Deng, Y. Hu, J. Zhou, L. Yu, T. Heine, X. Pan, X. Bao, Visualizing electronic interactions between iron and carbon by X-ray chemical imaging and spectroscopy, Chem. Sci. 6 (2015) 3262–3267.

[68] P. Heydari, A. Hafizi, M.R. Rahimpour, R. Khalifeh, Experimental investigation of improved graphene oxide as an efficient catalyst for the sustainable chemical fixation of CO_2 with epoxides, J. Environ. Chem. Eng. 8 (2020) 104568.

[69] S. Zhang, H. Zhang, F. Cao, Y. Ma, Y. Qu, Catalytic behavior of graphene oxides for converting CO2 into cyclic carbonates at one atmospheric pressure, ACS Sustain. Chem. Eng. 6 (2018) 4204–4211.

[70] A. Samikannu, L.J. Konwar, P. Maki-Arvela, J.-P. Mikkola, Renewable N-doped active carbons as efficient catalysts for direct synthesis of cyclic carbonates from epoxides and CO_2, Appl. Catal. B Environ. 241 (2019) 41–51.

[71] L. Guo, K.J. Lamb, M. North, Recent developments in organocatalysed transformations of epoxides and carbon dioxide into cyclic carbonates, Green Chem. 23 (2021) 77–118.

[72] Y. Ye, L. Liang, X. Zhang, J. Sun, Simple carbonaceous-material-loaded mesoporous SiO2 composite catalyst for epoxide-CO2 cycloaddition reaction, J. Colloid Interface Sci. 610 (2022) 818–829.

[73] L. Luo, C. Yang, F. Liu, T. Zhao, Heteroatom-N,S co-doped porous carbons derived from waste biomass as bifunctional materials for enhanced CO_2 adsorption and conversion, Sep. Purif. Technol. 320 (2023) 124090.

[74] C. Su, Y. Liu, Z. Luo, J.-P. Veder, Y. Zhong, S.P. Jiang, Z. Shao, Defects-rich porous carbon microspheres as green electrocatalysts for efficient and stable oxygen-reduction reaction over a wide range of pH values, Chem. Eng. J. 406 (2021) 126883.

[75] Q. Fan, C. Song, P. Fu, Advances in the improvement of the quality and efficiency of biomass-derived porous carbon: a comprehensive review on synthesis strategies and heteroatom doping effects, J. Clean. Prod. 452 (2024) 142169.

[76] H. Ming, J. Ming, W. Kwak, W. Yang, Q. Zhou, J. Zheng, Y. Sun, Fluorine-doped porous carbon-decorated Fe_3O_4-FeF_2 composite versus $LiNi_{0.5}Mn_{1.5}O_4$ towards a full battery with robust capability, Electrochim. Acta 169 (2015) 291–299.

[77] J. Zhou, J. Lian, L. Hou, J. Zhang, H. Gou, M. Xia, Y. Zhao, T.A. Strobel, L. Tao, F. Gao, Ultrahigh volumetric capacitance and cyclic stability of fluorine and nitrogen co-doped carbon microspheres, Nat. Commun. 6 (2015) 8503.